Dust shells around infrared carbon stars

M.A.T. Groenewegen[1,2]

[1] Astronomical Institute 'Anton Pannekoek', Kruislaan 403, NL-1098 SJ Amsterdam, The Netherlands
[2] present address: Institut d'Astrophysique de Paris, CNRS, 98 bis Bd. Arago, F-75014 Paris, France

Abstract. The spectral energy distributions (SEDs) and LRS spectra of 21 infrared carbon stars are fitted using a dust radiative transfer model. The parameters derived are the temperature of the dust at the inner radius (T_{inn}), the mass loss rate and the ratio of silicon carbide (SiC) to amorphous carbon (AMC) dust. Mass loss rates between a few 10^{-6} and $1.3 \, 10^{-4} \, M_{\odot} \, yr^{-1}$ are found. The SiC/AMC ratio and T_{inn} are found to decrease with increasing S_{25}/S_{12} ratio. The former correlation may be due to an increasing C/O ratio. The latter correlation may be due to the fact that dust growth continues until the density is too low. For increasing mass loss rates (i.e. larger S_{25}/S_{12} ratios) this leads to larger effective dust radii and hence to a decrease of T_{inn}.

The standard model with a constant mass loss rate and amorphous carbon dust (with $Q_{\lambda} \sim \lambda^{-\beta}$; $\beta \approx 1$ for $\lambda > 30 \, \mu m$) predicts too much flux at 60 and 100 μm compared to the observations. The discrepancy increases with the S_{25}/S_{12} ratio. This indicates that either $\beta > 1$ and/or that the mass loss rate has been lower in the past. Mass loss histories as proposed by Bedijn (1987) and related to thermal pulses are considered. An increase in the mass loss rate by a factor of 3-30 over the past 10^4 yrs or β's in the range 1.2-1.9 both fit the observed IRAS 60 and 100 μm flux-densities. Theoretically one expects that β decreases or remains constant as the dust continuum temperature decreases, contrary to the β's needed to fit the observed IRAS 60 and 100 μm flux-densities. This points to the mass loss histories rather than a steeper slope of the absorption coefficient to explain the observed 60 and 100 μm flux-densities, at least for the reddest stars in the sample. Both mass loss histories predict sub-mm fluxes in better agreement with observations than a large value for β. From the SEDs the precise form of the mass loss rate history can not be reconstructed. It is suggested that with mapping the circumstellar shell with $2''$ resolution in the far-infrared and sub-mm region this may become possible.

An excess emission above the dust emission and photospheric component is found at sub-mm wavelengths for all seven stars where sub-mm data is available. This is possibly due to free-free emission.

1. Introduction

One of the characteristics of AGB stars is their large mass loss rate. Dust grains form in the cool expanding circumstellar envelope, absorb optical radiation and re-emit it in the infrared. Previous studies of dust shells around AGB stars either concentrated on oxygen-rich Mira's and OH/IR stars (e.g. Rowan-Robinson & Harris 1983a; Bedijn 1987; Schutte & Tielens 1989; Justtanont & Tielens 1992; Griffin 1993) or on the well-known carbon star IRC 10 216 (e.g. Mitchell & Robinson 1980; Martin & Rogers 1987; Le Bertre 1987; Orofino et al. 1990; Griffin 1990).

Rowan-Robinson & Harris (1983b) considered a sample of 44 carbon stars but no IRAS and LRS data were available at the time. Rowan-Robinson et al. (1986) fitted the spectral energy distributions (SEDs) of five carbon stars fixing the dust temperature at the inner radius at 1000 K, and assuming a dust absorption law of $\sim\lambda^{-1}$ for all wavelengths without considering the presence of silicon carbide (which has a feature near 11.3 μm). Le Bertre (1988) fitted three carbon stars. Chan & Kwok (1990) fitted SEDs of 145 carbon stars with an LRS classification of 4n (indicating silicon carbide emission), and they therefore missed some carbon stars with weak silicon carbide emission (which sometimes have an LRS = 1n classification) and extreme carbon stars which have an LRS = 2n classification. They fixed the dust temperature at the inner radius at 1500 K and only included silicon carbide dust in their model.

In this paper an attempt will be made to study in some detail questions regarding the mass loss rate, the possible mass loss history, dust formation and strength of the silicon carbide feature. To this end fits are made to the spectral energy distributions and LRS spectra of 21 infrared carbon stars. The dust radiative transfer model used, allows for a time-dependent mass loss rate. The dust temperature at the inner radius, the mass loss rate and the ratio of the amount of silicon carbide to amorphous carbon dust are treated as free parameters. Recently acquired

broad-band data at optical (Groenewegen & de Jong 1993), near-infrared and sub-mm wavelengths (Groenewegen et al. 1993), and 2-4 μm spectra (Groenewegen et al. 1994) supplemented with data available in the literature are used to constrain the radiative transfer models. Preliminary results for three carbon stars were presented by Groenewegen & de Jong (1991).

In Sect. 2 the radiative transfer model is introduced. In Sect. 3 the fits to the SEDs and LRS spectra are presented and the results are discussed in Sect. 4.

2. The model

The radiative transfer model of Groenewegen (1993) is used. This model was developed to handle non-r^{-2} density distributions in spherically symmetric dust shells. It simultaneously solves the radiative transfer equation and the thermal balance equation for the dust.

The SED is determined by the dust optical depth, defined by:

$$\tau_\lambda = \int_{r_{inner}}^{r_{outer}} \pi a^2 Q_\lambda \, n_d(r) \, dr =$$

$$= 5.405 \; 10^8 \; \frac{\dot{M} \, \Psi \, Q_\lambda/a}{R_\star \, v_\infty \, \rho_d \, r_c} \int_1^{x_{max}} \frac{R(x)}{x^2} \, dx \qquad (1)$$

where $x = r/r_c$ and $\dot{M}(r) = \dot{M} \, R(x)$. The units are: the (present-day) mass loss rate at the inner radius $\dot{M}$ in $M_\odot \, yr^{-1}$, Ψ the dust-to-gas mass ratio, Q_λ/a the absorption coefficient of the dust over the grain radius in cm^{-1}, $R_\star$ the stellar radius in solar radii, v_∞ the terminal velocity of the circumstellar envelope in $km \, s^{-1}$, ρ_d the dust grain density in $gr \, cm^{-3}$, r_c the inner dust radius in stellar radii and x_{max} the outer radius in units of r_c. The normalised mass loss rate profile $R(x)$ should obey $R(1) = 1$. The velocity law is assumed to be constant in this paper. A dust-to-gas ratio of $\Psi = 0.005$ and a grain density of $\rho_d = 2.0$ g cm^{-3} are adopted. No specific grain size has to be adopted as long as it is sufficiently small so that Q_λ/a is independent of a. Scattering is neglected in the calculations. For IRC 10 216, Martin & Rogers (1987) derived $a < 0.1 \, \mu m$ from polarization measurements. For $a < 0.1 \, \mu m$, scattered light may become the dominant contribution to the SED for $\lambda \lesssim 0.7 \, \mu m$ (Martin & Rogers 1987; Le Bertre 1988). For this sample of infrared carbon stars this is of no practical importance. The outer radius is determined in the model by a dust temperature of 20 K. The main parameters in the model are the dust temperature at the inner radius (T_{inn}), the optical depth at some reference wavelength and the ratio of silicon carbide to amorphous carbon dust. The inner dust radius (r_c) and the temperature at the inner radius (T_{inn}) are uniquely related through the condition of radiative equilibrium. In Sect. 3 the mass loss rate is assumed to be constant, in Sect. 4 a time-dependent mass loss rate is considered.

The central star is represented by a blackbody modified to allow for the characteristic absorption feature in carbon stars at 3.1 μm:

$$B_\lambda(T_{eff}) \, \exp\left(-A \, e^{-\left(\frac{\lambda - \lambda_0}{\Delta\lambda}\right)^2}\right) \qquad (2)$$

with $\lambda_0 = 3.1 \, \mu m$. This novelty is introduced to be able to directly fit the observed 2-4 μm spectra of some stars. Following Groenewegen et al. (1994), $A = 4.605$ and $\Delta\lambda = 0.075 \, \mu m$ are adopted. A value of $A = 4.605$ means that in a star without a circumstellar shell the flux in the feature at 3.1 μm is 1% of the continuum. The effective temperatures and luminosities of Galactic carbon stars are poorly known. Canonical values of T_{eff} = 2500 K and $L = 7050 \, L_\odot$ are adopted throughout this paper (the mean luminosity of carbon stars in the LMC, Frogel et al. 1981); this implies $R_\star = 447 \, R_\odot$.

For the dust properties a combination of amorphous carbon (AMC) grains and silicon carbide (SiC) grains is assumed. For simplicity, one condensation temperature is used. In principle, SiC and AMC have different temperature profiles but to take this into account requires two additional free parameters (a second condensation temperature and a dust-to-gas ratio). Since the abundance of SiC is found to be small, the simplification of the temperature profile seems to be justified. In Eq. (1) the value of (Q_λ/a) is calculated from $(Q_\lambda/a) = x \, (Q_\lambda/a)^{SiC} + (1-x) \, (Q_\lambda/a)^{AMC}$ where $x \, (\in [0, 1])$ is determined by the fit to the LRS spectrum. The absorption coefficient for AMC is calculated from the optical constants listed in Rouleau & Martin (1991) for their AC1-species.

Absorption coefficients for several forms of SiC have been listed in the literature. Species considered here are SiC1200, SiC600, SiCN, β-SiC (all from Borghesi et al. 1985) and α-SiC (Pégourié 1988)[1]. To determine the most suitable choice some test runs were made fitting the SED and LRS spectrum of the star with one of the strongest SiC feature in the LRS atlas and with a high signal-to-noise, namely IRAS 17172–4020 (LRS classification 46). Figure 1 shows that α-SiC (Pégourié 1988) gives the best result. The absorption coefficient of α-SiC is adopted for silicon carbide from now on. Figure 2 shows the absorption coefficient (Q_λ/a) for pure AMC and for a mix (by mass) of 90% AMC and 10% SiC for the wavelength region 0.1 - 1000 μm.

Chan & Kwok (1990) concluded that the empirical opacity function they derived resembles that of β-SiC and suggested an evolution from α-SiC to β-SiC when a star evolves from an optical to an infrared carbon star. Unfortunately they did not publish any detailed fits to the LRS spectra of the stars in their

[1] For SiC1200, SiC600, SiCN and β-SiC the absorption coefficients in the range 2.5 to 40 μm are taken from Borghesi et al. (1985) applying matrix correction factors of $h = 0.46$ and $\Delta\lambda = -0.3$ (see their Table 4). For $\lambda > 40 \, \mu m$ the results of Blanco et al. (1991) are used for these species, scaled to 40 μm. For $\lambda < 2.5 \, \mu m$ the values of Pégourié (1988) are used, scaled at 2.5 μm. For α-SiC (Pégourié 1988) the data points beyond 250 μm are extrapolated using $Q_\lambda \sim \lambda^{-2.0}$, based on the last two data points listed by him.
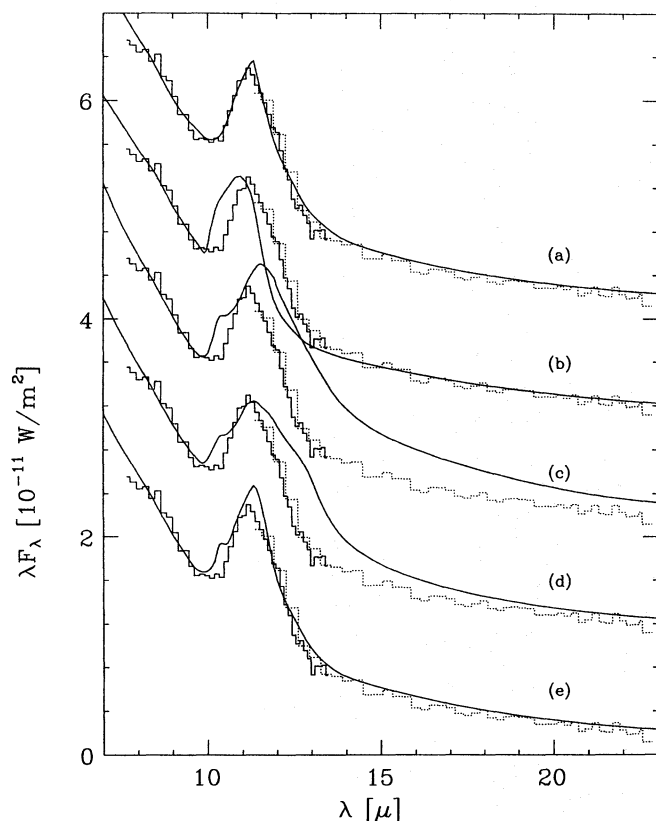
Fig. 1. The LRS spectrum of IRAS 17172−4020 fitted with different species of dust containing x% silicon carbide and $(100-x)$% amorphous carbon. From top to bottom: (a) α-SiC ($x = 10$), (b) β-SiC ($x = 15$), (c) SiCN ($x = 15$), (d) SiC1200 ($x = 10$) and (e) SiC600 ($x = 10$). The offset between each spectrum is one flux unit. Spectrum (e) has no offset
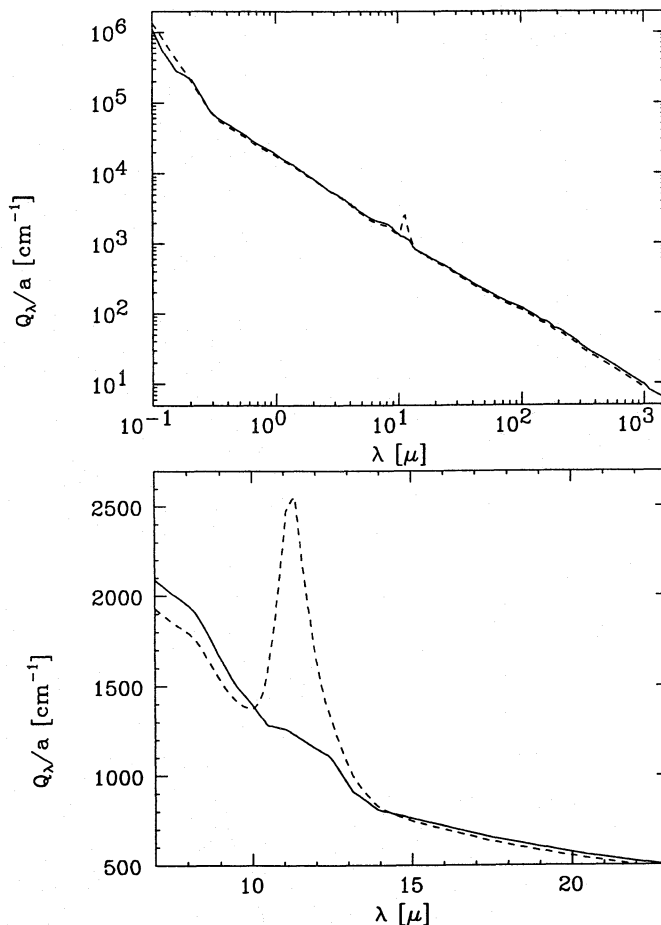

Fig. 2. The absorption coefficient of pure amorphous carbon dust (solid line) and a mixture of 90% amorphous carbon and 10% silicon carbide dust (dashed line)

sample. Our results show that excellent fits to most of the LRS spectra can be obtained with α-SiC (cf. Figs. 3-23). Only in the cases of IRAS 20396+4757 (Fig. 5) and IRAS 03229+4721 (Fig. 6) there is evidence for the presence of β-SiC. Previously, Baron et al. (1987) and Papoular (1988) also favoured α-SiC to explain the shape of the SiC feature.

In some stars to be discussed later a 30 μm emission feature has been observed (AFGL 489, 3068, 3116), in another star (AFGL 2632) such a feature is absent (Forrest et al. 1981; Goebel & Moseley 1985). The 30 μm feature is not taken into account. The 30 μm feature may contribute up to $\sim$30% of the IRAS 25 μm flux-density and up to $\sim$10% of the IRAS 60 μm flux-density.

Beam effects are taken into account. For $\lambda < 7$ μm and between 150 $\mu m < \lambda < 300$ μm a Gaussian beam with a FWHM (full width half maximum) of 20″ is assumed. Between 7 $\mu m < \lambda < 150$ μm the beam effects of the IRAS detectors is taken into account. The information on the spatial response of the IRAS detectors is taken from Table II.C.3, Table IV.A.1 and Fig. IV.A.3 of the *Explanatory Supplement* (Joint IRAS Science Working Group 1986). The beams of the 12 and 25 μm bands are taken to be rectangular with FWHM values of 60″

in the in-scan direction for both detectors. The beams of the 60 and 100 μm bands are taken to be Gaussian with in-scan FWHM values of 120″ and 220″ respectively. For $\lambda > 300$ μm the beam width of the JCMT telescope is assumed (FWHM = 18.5″). This allows a direct comparison with the observed sub-mm flux-densities in some of the program stars. The influence of beam effects is illustrated in Fig. 12 for AFGL 3116. The influence on the near-infrared and IRAS flux-densities is small. The main change is in the far-IR and mm-region.

In the models the calculated flux-density is convolved with the spectral response (Table II.C.5 of the *Explanatory Supplement*) to compare the predicted flux-densities directly to the flux-densities listed in the Point Source Catalog.

3. Fitting the SEDs

In Table 1 some general parameters are listed of the stars that are fitted. All are listed in Groenewegen et al. (1992; hereafter paper I), except IRAS 02345+5422 which is a very red carbon star that has a 12 μm flux-density of 33 Jy, below the limiting flux-density of 100 Jy considered in paper I. The sample is a selection of infrared carbon stars, ranging from stars with moderate mass

Table 1. The program stars

IRAS-name	AFGL	l	b	C_{21}	group[1]	A_V mag	v_∞[2] km s^{-1}	P[3] days	photometry[4]
11318−7256	4133	297.3	−11.2	−1.182	III	0.6	30.0		10, 11
14484−6152		316.6	−2.5	−1.138	IV	1.2	20.4		6, 9, 10
20396+4757	2632	86.5	3.8	−1.133	III	1.0	13.0	421 (1)	2, 8, 10, 14
03229+4721	489	148.2	−7.6	−1.076	III	0.9	16.5	535 (1)	2, 4, 10, 14, 17
07217−1246		228.1	1.2	−1.003	IV	1.9	28.5		6, 9, 10
15194−5115		325.5	4.7	−0.921	III	0.7	25.0	580 (3)	5, 10, 15, 19
07098−2012	1085	233.3	−4.8	−0.872	IV	1.0	23.8	725 (3)	9, 10, 15
16545−4214		343.5	0.3	−0.833	III	1.0	15.0:		9, 10, 12
06342+0328	971	208.2	−1.7	−0.796	IV	1.7	9.0	653 (3)	8, 9, 10, 12, 15
23320+4316	3116	108.5	−17.1	−0.777	III	0.5	14.5	620 (2)	3, 8, 10, 13, 14, 17
19321+2757	2417	62.6	4.0	−0.703	III	1.4	25.0	625 (2)	8, 10, 13, 20
09116−2439	5254	252.8	16.2	−0.667	IV	0.6	13.0		6, 7, 10
13477−6532	4183	309.0	−3.6	−0.389	IV	1.8	19.0		10
06012+0328	865	200.8	−7.0	−0.379	IV	1.2	16.5	696 (3)	10, 13, 15
19594+4047	2494	76.5	5.6	−0.286	IV	1.1	21.0	783 (2)	1, 10, 11, 13, 18
08074−3615		253.5	−1.8	−0.239	IV	2.6	19.0		10, 11
02345+5422	5076	138.1	−5.1	0.062	V	1.8	15.0:		11
08171−2134	5250	242.2	8.1	0.084	V	1.2	16.0		10
23166+1655	3068	93.5	−40.4	0.101	V	0.3	15.3	696 (3)	10, 11, 13, 15, 16, 21
21318+5631	5625	98.2	3.7	0.211	V	1.9	17.0		10
15471−5644		325.6	−2.2	0.382	V	2.8	15.0:		10

Notes. (1) Group designation of Groenewegen et al. (1992). (2) When no value could be found in the literature a value of 15.0 km s^{-1} has been assumed. These entries are flagged by a semicolon. (3) Between parentheses the references for the pulsation period: 1 = GCVS (Kholopov et al. 1985), 2 = Jones et al. (1990), 3 = Le Bertre (1992). (4) References for the photometry used in Sect. 3: 1 = Alknis (1980), 2 = Bergeat et al. (1976), 3 = Cohen & Kuhi (1977), 4 = Dyck et al. (1974), 5 = Epchtein et al. (1987), 6 = Epchtein et al. (1990), 7 = Fouqué et al. (1992), 8 = Grasdalen et al. (1983), 9 = Groenewegen & de Jong (1993), 10 = Groenewegen et al. (1993), 11 = Groenewegen et al. (1994), 12 = Guglielmo et al. (1993), 13 = Jones et al. (1990), 14 = Kholopov et al. (1985), 15 = Le Bertre (1992), 16 = Lebofsky & Rieke (1977), 17 = Lockwood (1974), 18 = Low et al. (1976), 19 = Meadows et al. (1987), 20 = Noguchi et al. (1981), 21 = Sopka et al. (1985). In addition the IRAS flux-densities and the LRS spectra, corrected according to Cohen et al. (1992), are used.

loss rates to the most reddest carbon stars known. The stars have been selected for the availability of as many flux determinations over as large a wavelength region as possible.

Table 1 lists the IRAS-name and AFGL number, the galactic coordinates, the C_{21} ratio (defined as $2.5 \log(S_{25}/S_{12})$; the stars are listed in order of increasing C_{21}), the group designation of paper I, the interstellar extinction in the V-band (see below), the terminal velocity of the envelope (see below), the pulsation period either from optical or infrared light curves and finally the references to the photometry used to construct the SEDs.

The interstellar extinction at V is estimated from the extinction maps of Neckel & Klare (1980; for $|b| \lesssim 7.6^0$), which list observed values of A_V as a function of galactic coordinates and distance, and the Parenago (1940) model for the interstellar extinction (see paper I for the exact form). For the distance the value in Table 2 is used. Both estimates for A_V usually agree and the average value is quoted in Table 1. The terminal velocities can be accurately determined from millimeter observations. The values in Table 1 are taken from the CO and HCN catalog of Loup et al. (1993) or from Groenewegen et al. (in preparation).

The fitting procedure is as follows. Typically four values for the dust temperature at the inner radius (T_{inn}) are chosen.

The mass loss rate (assumed constant) is varied to fit the SED. The distance is determined by demanding that the predicted and observed IRAS 25 μm flux-density agree. The SiC feature is fitted by changing the (mass) ratio SiC/AMC. This last step is straightforward since the strength of the SiC feature turns out to scale linearly with the adopted SiC/AMC ratio. In choosing the best value for T_{inn} equal weight is given to the fits of the SED and the LRS spectrum (and the observed 2-4 μm spectrum, when available). If necessary, the above mentioned steps are repeated for the final choice of T_{inn}. The formal errors in the mass loss rate and T_{inn} are estimated to be 20% (3σ). The best-fitting models are shown in Figs. 3 to 23 and the corresponding model parameters are listed in Table 2.

For some stars fairly low values of T_{inn} are needed to fit the SED. For four stars (Figs. 16, 18, 19 and 22) model results for larger values of T_{inn} are also shown (see Table 2 for the corresponding model parameters) to illustrate the sensitivity of the fits to T_{inn}. The fits to the SEDs, LRS spectra and 2-4 μm spectra (when available) with the higher value of T_{inn} are clearly less good. For some of the reddest stars, the low value of T_{inn} found in combination with an adopted effective temperature of 2500 K results in fairly large values of the inner dust radius (cf.

Table 2. The fit parameters

IRAS-name	T_{inn} (K)	$\dot{M}$ ($M_\odot$ yr^{-1})	r_{inner} (R_*)	SiC/AMC	d (kpc)	$\tau_{11.33}$	$\tau_{0.5}$	remarks
11318−7256	1500	$4.0\ 10^{-6}$	2.3	0.07	0.67	0.37	6.49	
14484−6152	1100	$1.8\ 10^{-5}$	5.6	0.05	0.91	0.90	18.2	
20396+4757	1200	$2.7\ 10^{-6}$	3.9	0.06	0.55	0.33	6.12	
	1200	$2.4\ 10^{-6}$	2.2	0.06	0.53	0.33	6.12	T_{eff} = 2000 K
03229+4721	1000	$6.0\ 10^{-6}$	6.1	0.06	0.72	0.37	6.86	
07217−1246	1100	$1.4\ 10^{-5}$	5.2	0.03	1.79	0.48	11.3	
15194−5115	1100	$1.4\ 10^{-5}$	5.2	0.03	0.50	0.52	12.5	
07098−2012	1000	$5.5\ 10^{-6}$	6.2	0.05	1.07	0.39	7.91	
16545−4214	1300	$2.7\ 10^{-6}$	3.2	0.03	0.61	0.27	6.50	
06342+0328	1100	$6.5\ 10^{-6}$	5.4	0.05	1.15	0.76	15.4	
23320+4316	900	$1.5\ 10^{-5}$	8.5	0.03	0.68	0.60	14.2	
19321+2757	900	$1.2\ 10^{-5}$	7.9	0.03	0.87	0.30	7.14	
09116−2439	1100	$1.9\ 10^{-5}$	6.1	0.05	0.84	1.38	27.8	
13477−6532	800	$3.8\ 10^{-5}$	11.7	0.05	1.81	0.98	19.8	
06012+0328	800	$4.5\ 10^{-5}$	11.8	0.02	1.24	0.82	21.4	best fit
	1100	$3.5\ 10^{-5}$	6.3	0.02	1.17	1.19	31.0	
19594+4047	900	$3.3\ 10^{-5}$	8.9	0.05	1.05	1.00	20.3	
08074−3615	650	$9.1\ 10^{-5}$	19.8	0	2.11	0.90	28.9	best fit
	1100	$7.5\ 10^{-5}$	7.6	0	2.08	1.94	62.4	
02345+5422	650	$7.5\ 10^{-5}$	19.9	0	3.99	0.93	30.0	best fit
	1100	$5.5\ 10^{-5}$	7.4	0	3.80	1.83	58.9	
08171−2134	700	$1.3\ 10^{-4}$	18.3	0	2.42	1.65	53.3	
23166+1655	650	$1.0\ 10^{-4}$	20.5	0	0.93	1.19	38.1	
	650	$9.1\ 10^{-5}$	11.9	0	0.90	1.19	38.1	T_{eff} = 2000 K
21318+5631	700	$1.1\ 10^{-4}$	17.7	0	1.47	1.36	43.7	best fit
	1100	$8.0\ 10^{-5}$	7.9	0	1.39	2.23	71.5	
15471−5644	700	$8.5\ 10^{-5}$	17.4	0	1.73	1.21	38.9	

Table 2). One may question the reality of this. However, one must bear in mind that by lowering the effective temperature smaller inner radii can be obtained (see discussion below). The fact that the reddest stars would require the lowest effective temperatures to obtain a given value for the inner dust radius seems not inconsistent, as evolutionary tracks for AGB stars generally evolve to cooler temperatures.

The observed SEDs plotted in Figs. 3-23 have not been corrected for interstellar extinction. Reddening vectors are indicated in Figs. 3-23 for the shortest observed wavelength point based on the A_V's is Table 1 and the interstellar extinction curve of Cardelli et al. (1988). The correction for interstellar extinction is usually small compared to the variation in the SEDs due to variability.

Inspection of Figs. 3-23 shows that the quality of the fits to the SEDs and LRS spectra is high with only a few exceptions (notably 08074−3615 and 08171−2134, Figs. 18 and 20). In these cases the poor fit may be due to the fact that only one set of near-IR photometry is available, which makes it uncertain how to join the IRAS data with the near-IR data. When near-IR photometry at minimum and maximum light is available it is possible to estimate the effective phase which the IRAS observations represent.

The fits to the 2-4 μm spectra ranges from poor (e.g. 11318−7256, Fig. 3) to excellent (e.g. 13477−6532, Fig. 15). In the stars where there is disagreement the predicted strength of the 3.1 μm feature is always too small. This is not due to an underestimate of the strength of the 3.1 μm feature in the central star as this was already adopted to be strong (cf. Eq. 2). The discrepancy may point to an additional contribution of circumstellar 3.1 μm absorption (see the discussion in Groenewegen et al. 1994). Part of the discrepancy may in some cases also be due to the difference in phase between the different observations. It would be interesting to monitor the 2-4 μm region during a pulsation period in a few stars to investigate how large the changes in the continuum and the 3.1 μm feature are. In the cases that no observed 2-4 μm spectra are available, the line profiles are a prediction of the expected strength.

The derived mass loss rates are subject to the following systematic effects. Following Eq. (1) the mass loss rate scales like $\sim R_* v_\infty/\kappa$, where κ is the dust opacity. For a constant effective temperature, the derived mass loss rates (and derived distances) scale like $\sqrt{L}$. The opacity at 60 μm for the adopted absorption coefficient ($\kappa = 3\ Q/4\ a\ \rho_d$) is 68 cm^{2}gr^{-1}. This is about a factor of 2 lower than the usually quoted value of $\sim$160 cm^{2}gr^{-1} (see e.g. Jura 1986). Since the mass loss rate scales
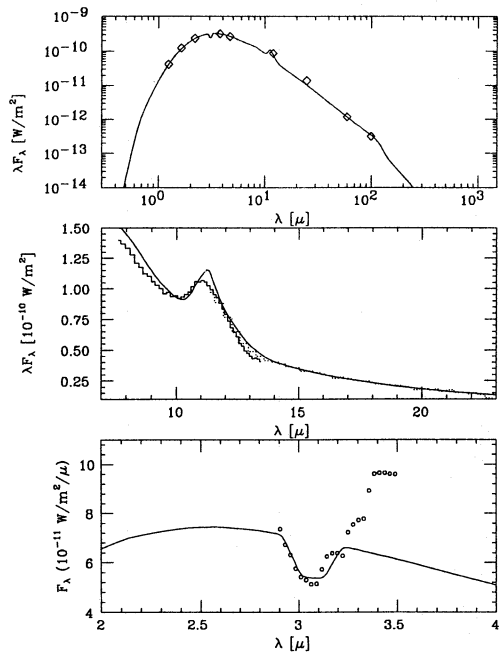
Fig. 3. The fit to the SED, LRS spectrum and 2-4 μm region of IRAS 11318−7256. For the corresponding parameters see Table 2. The remaining part of this caption refers to Figs. 3-23 in general. The model is represented by the solid line, the observations by the symbols and the ragged lines. The sub-mm and the most uncertain optical and near-IR data points have errorbars. Observations at minimum and maximum light are connected. Upperlimits are indicated by a $\vee$. The line near 1 μm represents the reddening vector at the shortest observed wavelength point (see Table 1). The predicted LRS spectrum and 2-4 μm spectrum are scaled to the observations. The scaling factor f (in the sense that the plotted model flux equals the calculated model flux multiplied by f) is 1.075 for the LRS spectrum and 0.675 for the 2-4 μm spectrum. The breaks in the models near 100 and 300 μm are due to beam effects (see Sect. 2)

like $1/\kappa$, the values quoted in Table 2 may be systematically too high by about a factor of 2.

The influence of the adopted effective temperature of the underlying central star on the SED is explicitly verified in the cases of AFGL 2632 and AFGL 3068, where a model with T_{eff} = 2000 K is run (see Table 2). The influence of the effective temperature is twofold. Firstly, there is a direct effect in the stellar contribution to the emerging flux. For most infrared stars (like AFGL 3068) this effect is negligible since the stellar flux is completely reprocessed in the dust shell. Secondly, the effective temperature influences the temperature distribution of the dust (through the equation of radiative equilibrium). To obtain optical depths equal to that for the standard model with T_{eff} = 2500 K, the mass loss rates need to be changed by $\lesssim 10\%$ and the distances need to be changed by $\lesssim 5\%$ in those two cases. The decrease in the V-magnitude for AFGL 2632 is 1.9, indicating that for optical carbon stars and carbon stars with optical thin envelopes the uncertainty in the adopted effective temperature affects the fit of the SED in the optical part of the spectrum. The main change with respect to the standard model is in the
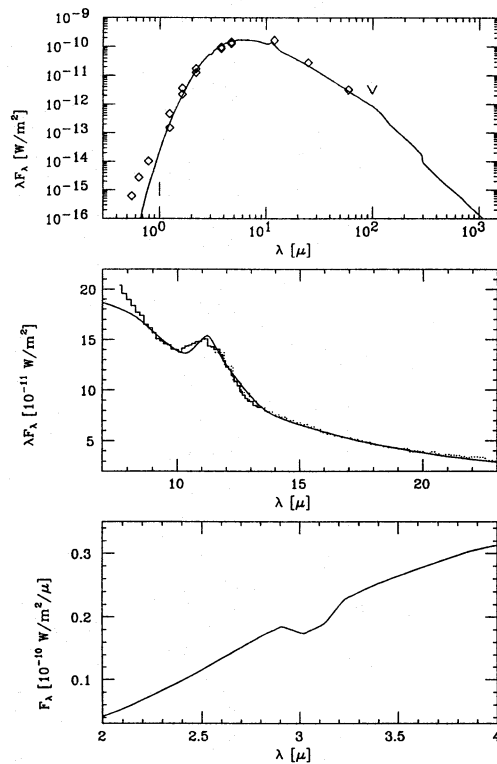
Fig. 4. As Fig. 3 for IRAS 14484−6152. The scaling factor for the LRS spectrum is 1.104
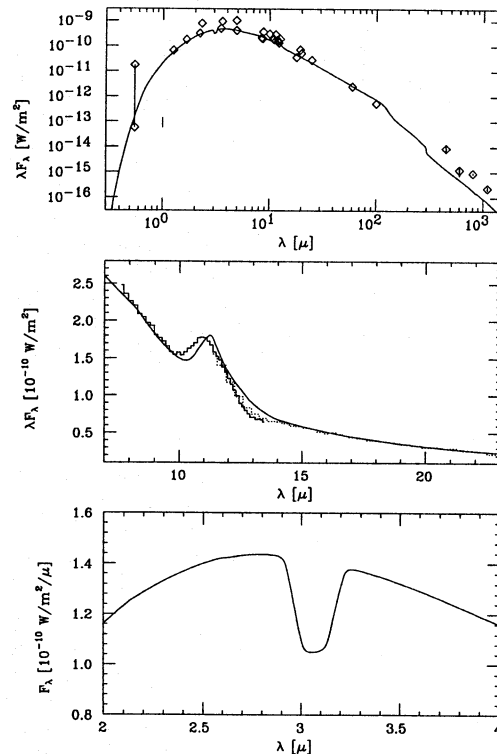

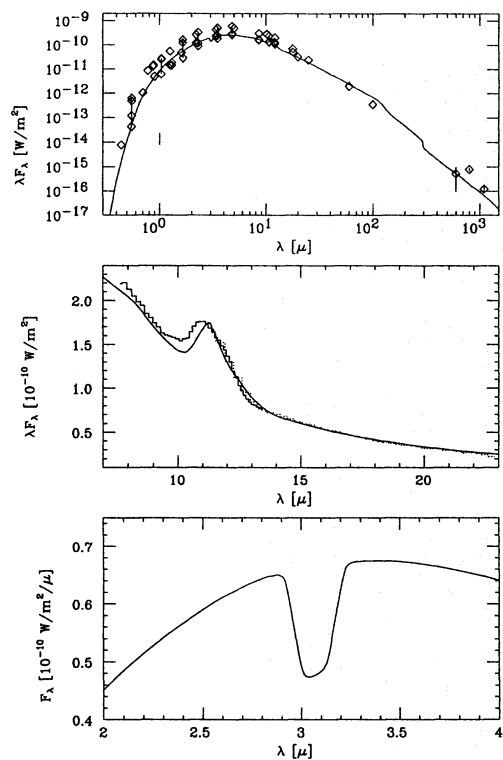**Fig. 5.** As Fig. 3 for IRAS 20396+4757. The scaling factor for the LRS spectrum is 0.888

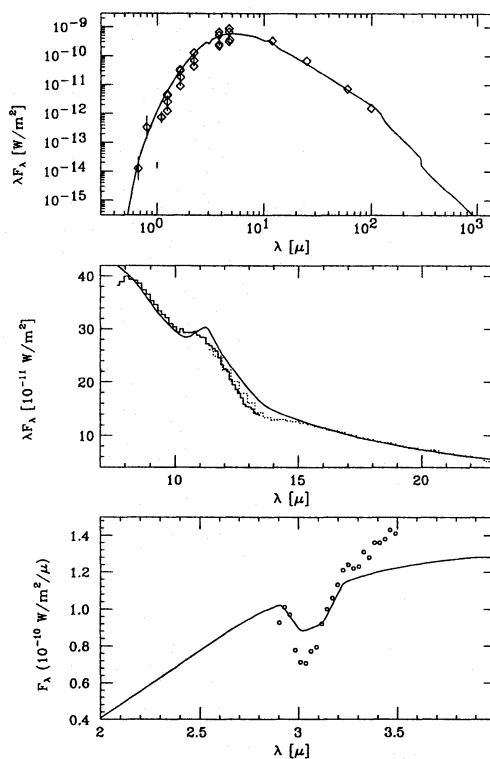**Fig. 6.** As Fig. 3 for IRAS 03229+4721. The scaling factor for the LRS spectrum is 1.097

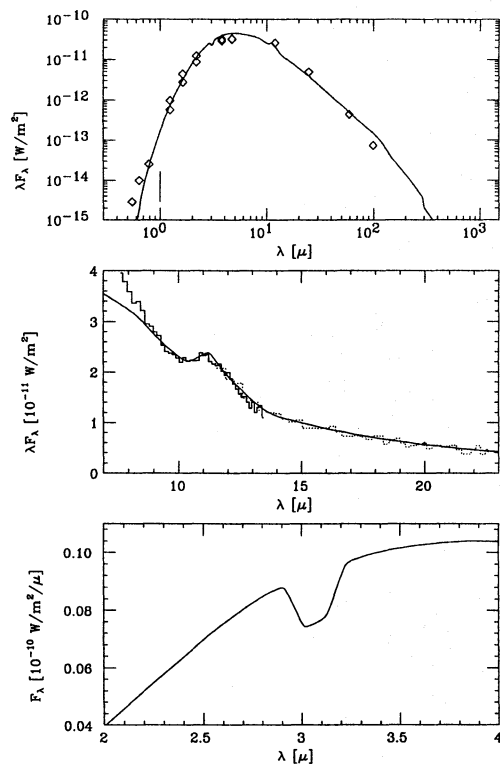**Fig. 8.** As Fig. 3 for IRAS 15194−5115. The scaling factor for the LRS spectrum is 0.86

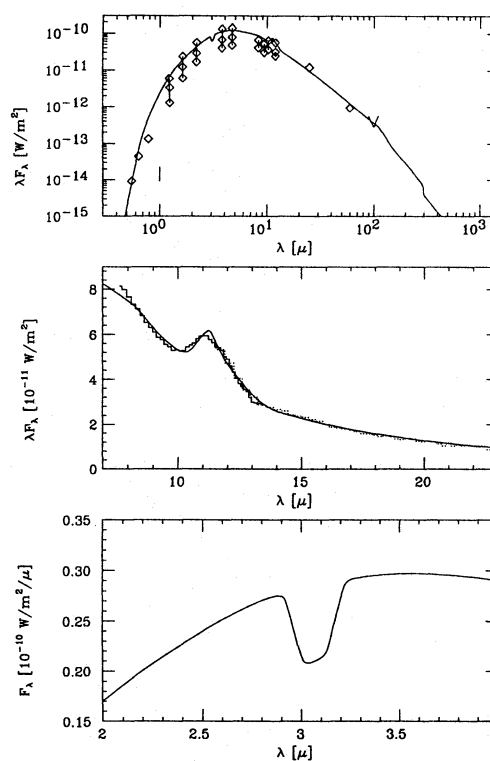**Fig. 7.** As Fig. 3 for IRAS 07217−1246. The scaling factor for the LRS spectrum is 0.906

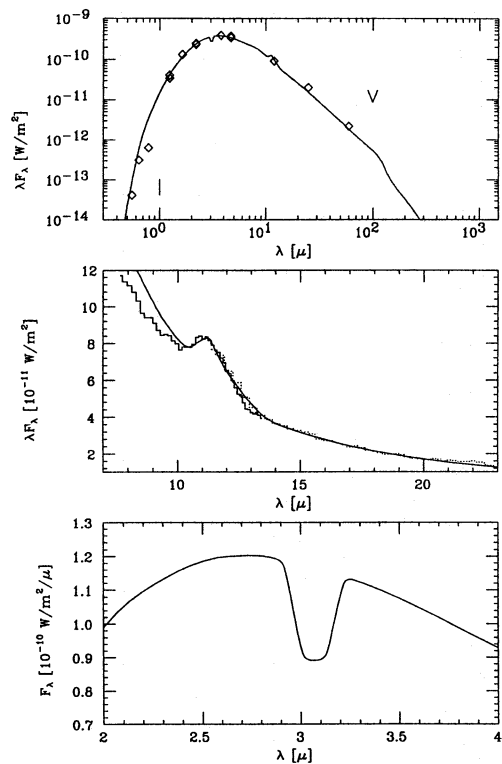**Fig. 9.** As Fig. 3 for IRAS 07098−2012. The scaling factor for the LRS spectrum is 0.821

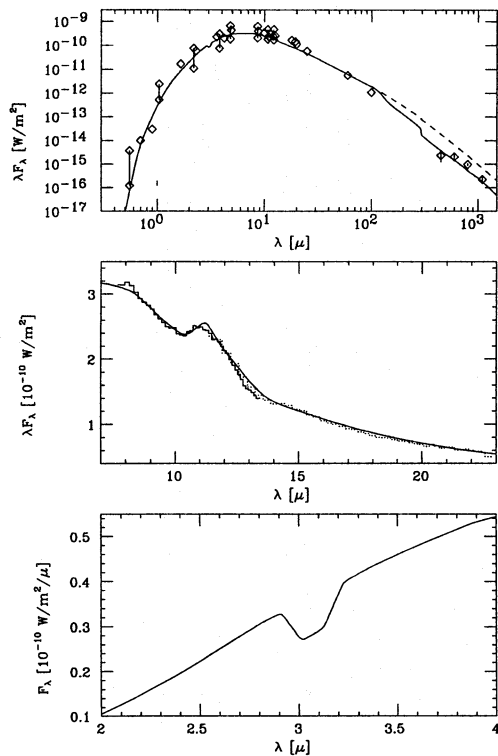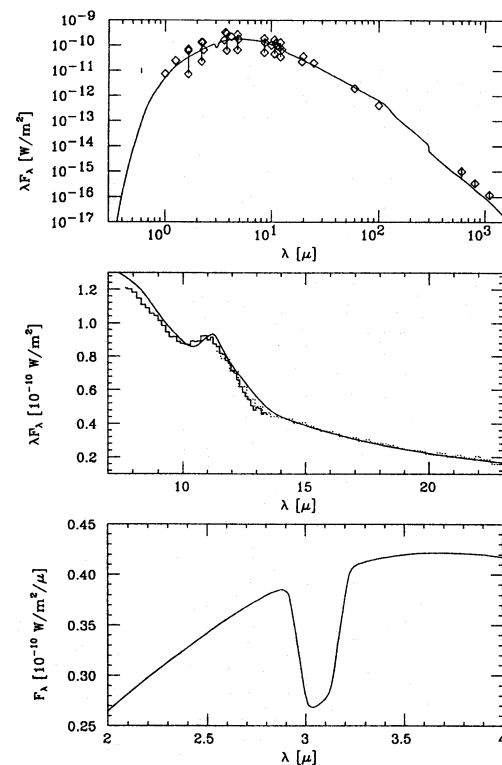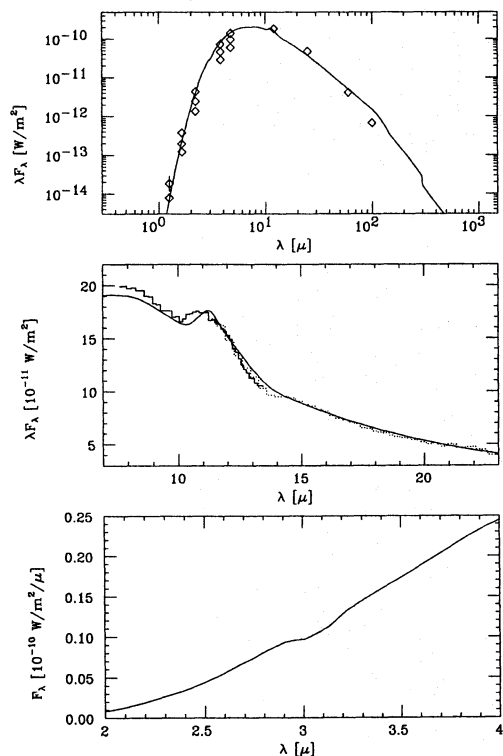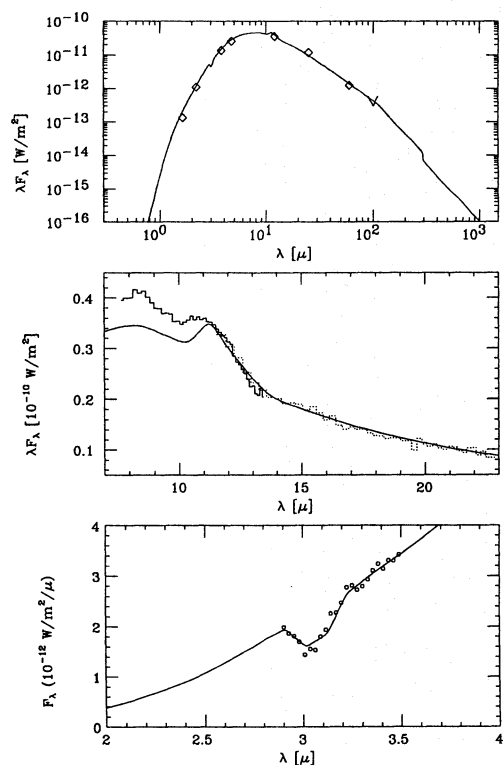**Fig. 10.** As Fig. 3 for IRAS 16545−4214. The scaling factor for the LRS spectrum is 0.665

Fig. 12. As Fig. 3 for IRAS 23320+4316. The scaling factor for the LRS spectrum is 1.00. The dashed line is the same model without beam effects
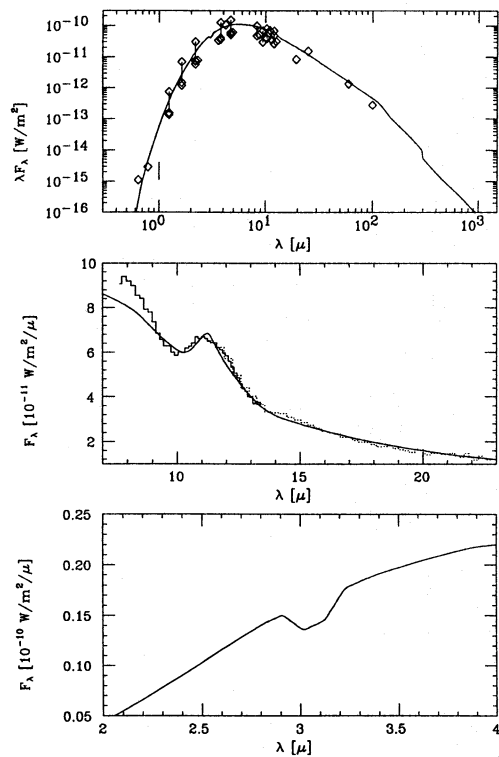
Fig. 11. As Fig. 3 for IRAS 06342−0328. The scaling factor for the LRS spectrum is 0.837

Fig. 13. As Fig. 3 for IRAS 19321+2757. The scaling factor for the LRS spectrum is 0.85

Fig. 14. As Fig. 3 for IRAS 09116−2439. The scaling factor for the LRS spectrum is 0.928

Fig. 16. As Fig. 3 for IRAS 06012+0328. The solid line is the best-fitting model with T_{inn} = 800 K. The scaling factor for the LRS spectrum is 0.800. The dashed line represents a model with T_{inn} = 1100 K

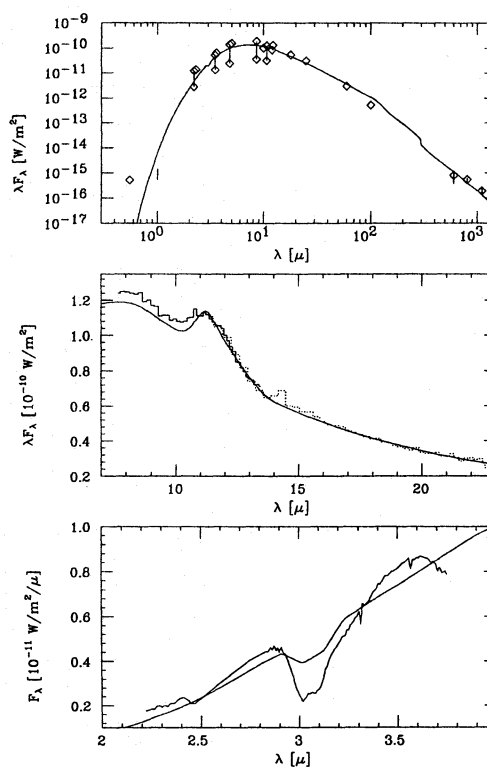**Fig. 15.** As Fig. 3 for IRAS 13477−6532. The scaling factor for the LRS spectrum is 1.097, for the 2-4 μm spectrum 0.758

Fig. 17. As Fig. 3 for IRAS 19594+4047. The scaling factor for the LRS spectrum is 0.882, for the 2-4 μm spectrum 0.612
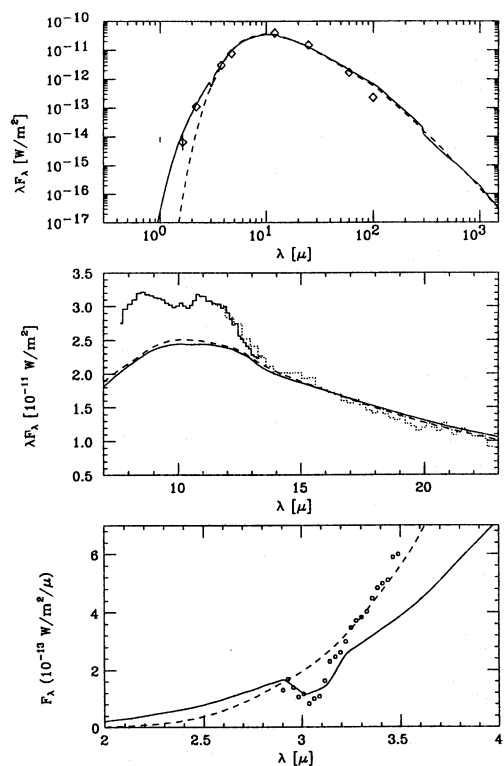
Fig. 18. As Fig. 3 for IRAS 08074−3615. The solid line is the best-fitting model with $T_{inn} = 650$ K. The scaling factor for the LRS spectrum is 0.707, for the 2-4 μm spectrum 0.640. The dashed line represents a model with $T_{inn} = 1100$ K
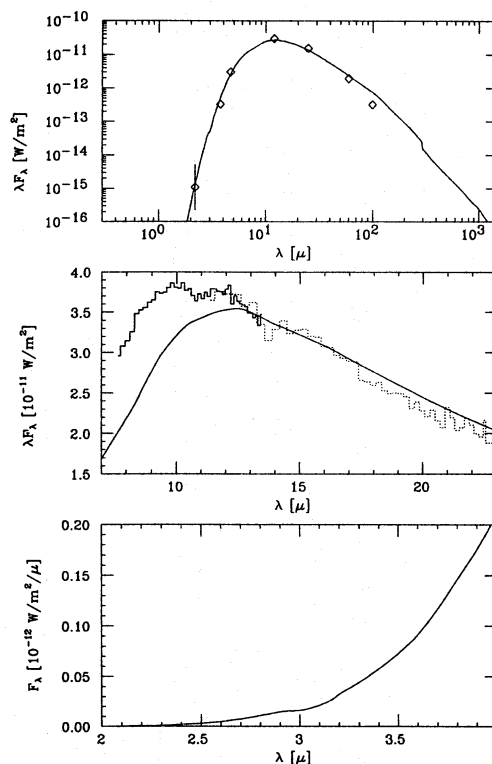
Fig. 20. As Fig. 3 for IRAS 08171−2134. The scaling factor for the LRS spectrum is 1.314

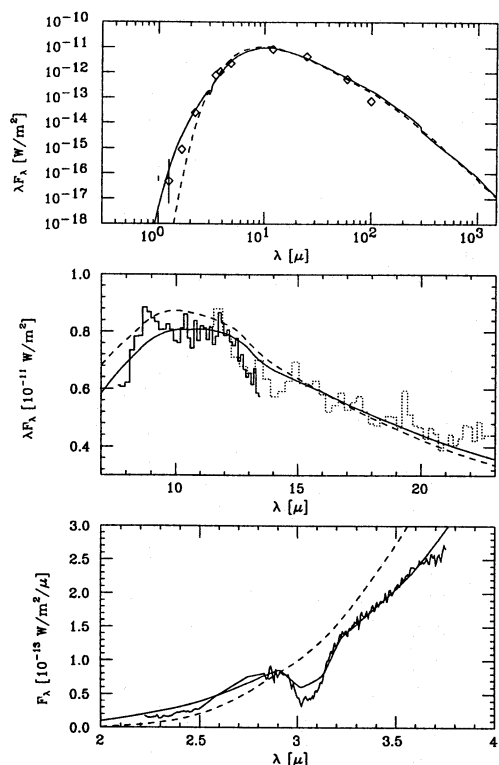**Fig. 19.** As Fig. 3 for IRAS 02345+5422. The solid line is the best-fitting model with $T_{inn} = 650$ K. The scaling factor for the LRS spectrum is 0.833, for the 2-4 μm spectrum 1.357. The dashed line represents a model with $T_{inn} = 1100$ K
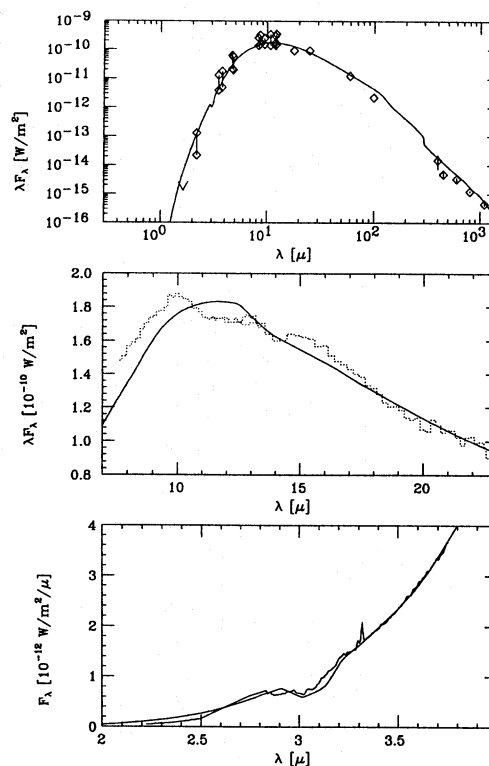
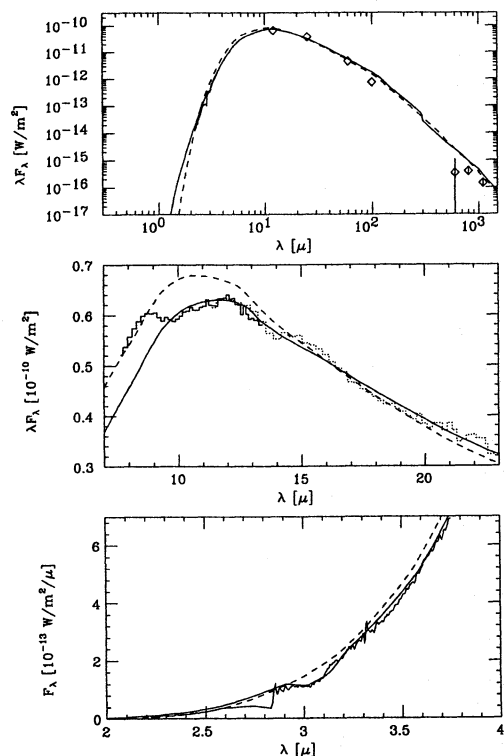**Fig. 21.** As Fig. 3 for IRAS 23166+1655. The scaling factor for the 2-4 μm spectrum is 1.79

Fig. 22. As Fig. 3 for IRAS 21318+5631. The solid line is the best-fitting model with T_{inn} = 700 K. The scaling factor for the LRS spectrum is 0.86. The dashed line represents a model with T_{inn} = 1100 K
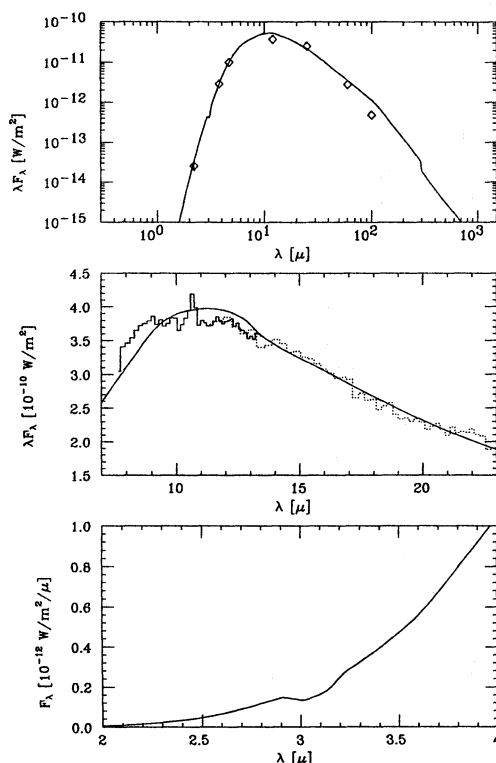

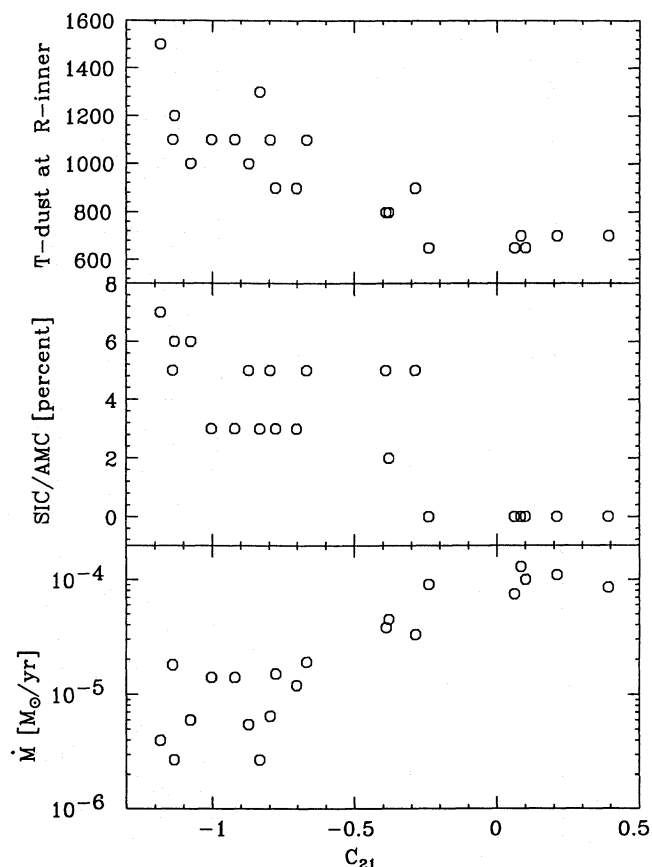**Fig. 23.** As Fig. 3 for IRAS 15471−5644. The scaling factor for the LRS spectrum is 0.759

Fig. 24. The dust temperature at the inner radius, the ratio of silicon carbide to amorphous carbon dust and the mass loss rate plotted versus $C_{21} = 2.5 \log(S_{25}/S_{12})$

inner dust radius which changes according to $r_{inner} \sim T_{eff}^{2.5}$ for amorphous carbon dust.

The ratio (by mass) of silicon carbide dust to amorphous determined is listed in Table 2. This ratio depends on the adopted absorption coefficients for SiC and AMC. Groenewegen & de Jong (1991), who used an opacity for AMC about 5 times higher than in the present study, derived SiC/AMC = 0.4 for 11318−7256, while I find a ratio of 0.07. Egan & Leung (1991) adopt SiC/AMC = 0.07 in their analysis of optical carbon stars without commenting on their particular choice. Egan & Leung use the same opacity for SiC and a similar one for AMC as in this study. The ratio they find for optical carbon stars agrees well with the ratio found in the least obscured stars in the present sample.

4. Discussion and conclusion

4.1. Dust properties

In Fig. 24 the derived quantities T_{inn}, the ratio of SiC to AMC and the mass loss rate are plotted as a function of C_{21}. The mass loss rate increases from a few 10^{-6} M$_\odot$ yr^{-1} to $\sim 1 \ 10^{-4}$ M$_\odot$ yr^{-1} for the most extreme carbon stars. Both the temperature of the dust at the inner radius and the ratio SiC/AMC decrease with increasing C_{21}. The dust temperature at the inner radius is
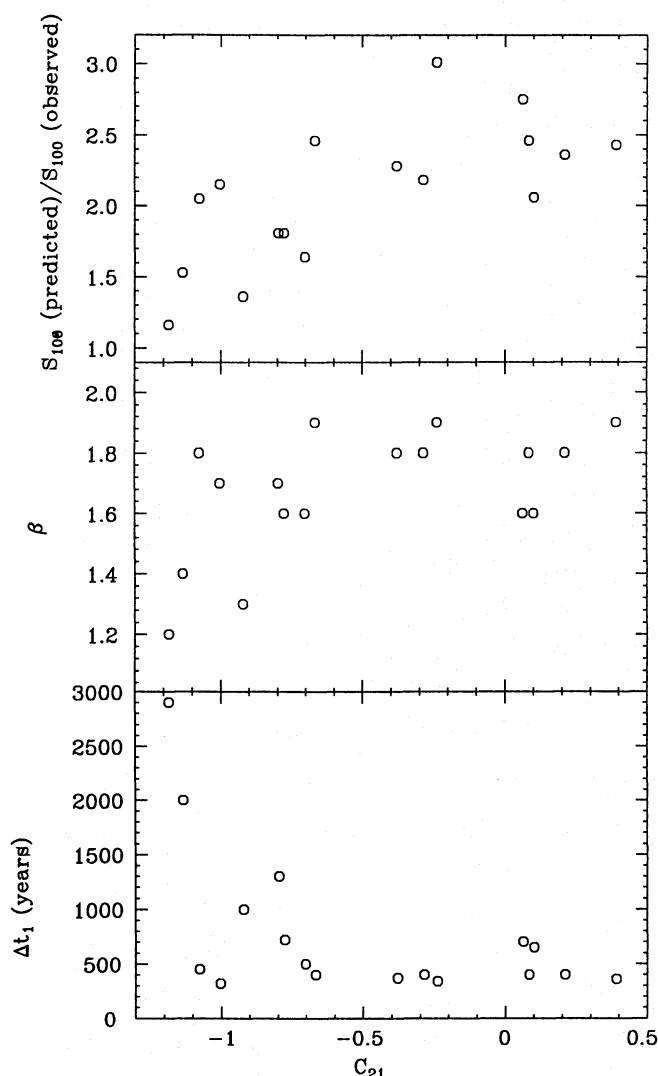
Fig. 25. The ratio of the predicted and observed flux-densities at 100 μm as a function of C_{21} for the standard model with a constant mass loss rate and a wavelength dependence of the absorption coefficient ($Q_\lambda \sim \lambda^{-\beta}$ for $\lambda \gtrsim 30 \, \mu m$) of $\beta = 1$ (top panel). The observed IRAS 60 and 100 μm flux-densities can be fitted using either a larger value for β (middle panel) or a mass loss rate where the mass loss rate is lower by a factor of 30, Δt_1 years ago (bottom panel). Details are given in the text

$T_{inn} = 1000$ K. Chan & Kwok (1990), who adopted $T_{inn} = 1500$ K, obtained a very poor fit to the SED of IRC 10 216. In a recent paper, Lopez et al. (1993) obtained $T_{inn} = 900$ K for IRAS 15194-5115 (assuming $T_{eff} = 2200$ K). The inner dust radius of 6 $R_\star$ they derive is in good agreement with my estimate of 5.2 $R_\star$. A value of $r_{inner} = 6 \, R_\star$ would be achieved with $T_{inn} \approx 1040$ K (when $T_{eff} = 2500$ K), while the best fit is obtained with $T_{inn} = 1100$ K. A difference of 60 K in T_{inn} is well within the errors.

The assumption of an unique inner dust shell radius is an oversimplification of the dust formation and growth process around long-period variables (LPVs). This has been studied theoretically, most recently by Fleischer et al. (1992) who show that the dust-to-gas ratio is a complicated function of radius, due to the periodic generation of shock waves. The derived inner dust radius should therefore be considered as the characteristic radius at which the dust formation has essentially been completed. While the mass loss rates differ by almost a factor of 50 in the sample, the density at the inner dust radius ($\rho_{inner} \sim \dot{M}/v_\infty r_{inner}^2$) varies by less than a factor of 4. This suggests that the density beyond a certain radius is too low for further dust formation. This radius effectively corresponds to the inner radius derived here. For larger mass loss rates (larger C_{21}) this critical density is reached at larger radii and hence at lower dust temperatures. This may explain the variation of T_{inn} with C_{21} in the top panel of Fig. 24. One might envision the following dust formation scenario. Condensation probably starts near the typical condensation temperature (~ 1500 K) fairly close to the star. The carbon (or SiC) dust grains that are formed are probably small and do not absorb (Tielens 1990) and therefore do not affect the observed SED. At larger radii the dust grains have become larger and now have typical absorption properties. The dust-to-gas ratio has increased. The process of dust formation and growth continues until the density is too low for further dust formation. Unfortunately, it is difficult to quantify this any further due to sensitivity of the inner dust radius to the adopted effective temperature.

The decrease in strength of the silicon carbide feature with increasing optical depth (cf. Fig. 24 middle panel) had already been noticed by Baron et al. (1987), Van der Bliek (1988), Chan & Kwok (1990), and in paper I. Although optical depth effects play a role it is demonstrated here that the weakening of the SiC feature is also an abundance effect and not only an optical depth effect.

Because silicon is depleted in the gas phase it has been inferred that practically all silicon is in grains (Sahai et al. 1984). Since silicon is not involved in any nuclear reactions, this suggests that the decrease of the SiC/AMC ratio is either a sequence of decreasing metallicity of the progenitor of the carbon star or a sequence of increasing C/O ratio. The latter possibility derives from the fact that, with nearly all oxygen tied up in CO, the number of carbon atoms to form dust (and molecules like HCN and C_nH_m) depends on (C/O–1). A sequence of decreasing metallicity is unlikely since carbon stars are probably formed from stars $\gtrsim 1.5 \, M_\odot$ (lifetime $\lesssim 3$ Gyr). In such relatively young stars the metallicity is expected to be close to solar.

for most stars considerably below the canonical condensation temperature of carbon-rich dust (~ 1500 K). A similar effect was found by Onaka et al. (1989) from fitting dust shell models to the LRS spectra of about 100 optically-bright oxygen-rich Mira variables. They explained this in terms of variations in the location of dust formation related to stellar pulsation.

Also for some infrared carbon stars values of T_{inn} below the condensation temperature are reported in the literature. The best studied case is IRC 10 216. From interferometric observations in the 1.6-5 μm region Ridgway & Keady (1988) derived $T_{inn} = 1040 \pm 100$ K. This value is also found by fitting the SED: Le Bertre (1988) derived $T_{inn} \approx 950$ K and Griffin (1990) found

23320+4316

If the sequence of decreasing SiC/AMC ratio were indeed a sequence of increasing C/O ratio then one could argue that this would also be a sequence of increasing initial mass, since more massive stars are expected to experience more thermal pulses as carbon stars, resulting in larger C/O ratios.

4.2. The mass loss history and long-wavelength dependence of the dust opacity

Inspecting Figs. 3-23 closely, reveals that the best-fitting models predict too much flux at 100 μm (and to a lesser extent also at 60 μm). This excess is also present when a different value for $T_{\rm inn}$ is adopted (see Figs 16, 18, 19 and 22). The ratio of the predicted to the observed 100 μm flux-density is smallest (1.2) in 11318-7256 and largest (3.0) in 08074-3615. There may be a correlation with C_{21} (Fig. 25, top panel). There are two possible explanations. The wavelength dependence of the absorption coefficient ($Q_\lambda \sim \lambda^{-\beta}$) is steeper for $\lambda \gtrsim 30\,\mu m$ than adopted in this study for the amorphous carbon dust species, and/or the mass loss rate has been lower in the past.

Two mass loss histories are considered here. The first mass loss history is that proposed by Bedijn (1987) where the mass loss rate at the tip of the AGB varies like:

$$\dot{M}(t) = \frac{\dot{M}_0}{(1 - t/t_0)^\alpha} \qquad (t < t_0) \qquad (3)$$

Suppose the mass loss rate has increased by a factor of f in the last Δt years and the present-day (time t_1) mass loss rate is $\dot{M}_1$. These parameters are related to $\dot{M}_0$ and t_0 as follows:

$$
\begin{aligned}
t_0 &= t_1 + \frac{\Delta t}{f^{1/\alpha} - 1} \\
\dot{M}_0 &= \dot{M}_1\, t_0^{-\alpha}\,\left(\frac{\Delta t}{f^{1/\alpha} - 1}\right)^\alpha
\end{aligned}
\qquad (4)
$$

Values for α between 0.5 and 1 have been proposed in the literature (Baud & Habing 1983; Bedijn 1987; van der Veen 1989). In the following calculations $\alpha = 0.75$ is used, expecting that the results are qualitatively similar for $\alpha = 0.5$ or 1. The relevant time scales are the flow time scale through the envelope and $\dot{M}/\ddot{M}$. For the models in the previous section the time for a dust particle to travel from the inner to the outer radius is $\sim 3.5 \cdot 10^4$ yrs. The relevant time scale on which the mass loss rate must change to give appreciable changes in the SED is therefore shorter than this and in the present study adopted to be $\Delta t = 10^4$ yrs.

The second mass loss history considered here is a sudden increase in the mass loss rate by a factor of f_1, Δt_1 years ago. Such a mass loss history is suggested by the observation that some AGB stars make loops in the IRAS color-color-diagram (Willems & de Jong 1988; Zijlstra et al. 1992) indicating that the mass loss rate depends on the phase in the thermal-pulse cycle (cf. Groenewegen & de Jong 1994). Based on theoretical arguments a ratio of the mass loss rate in the quiescent hydrogen-burning phase to that in the luminosity dip is adopted of $f_1 = 30$.
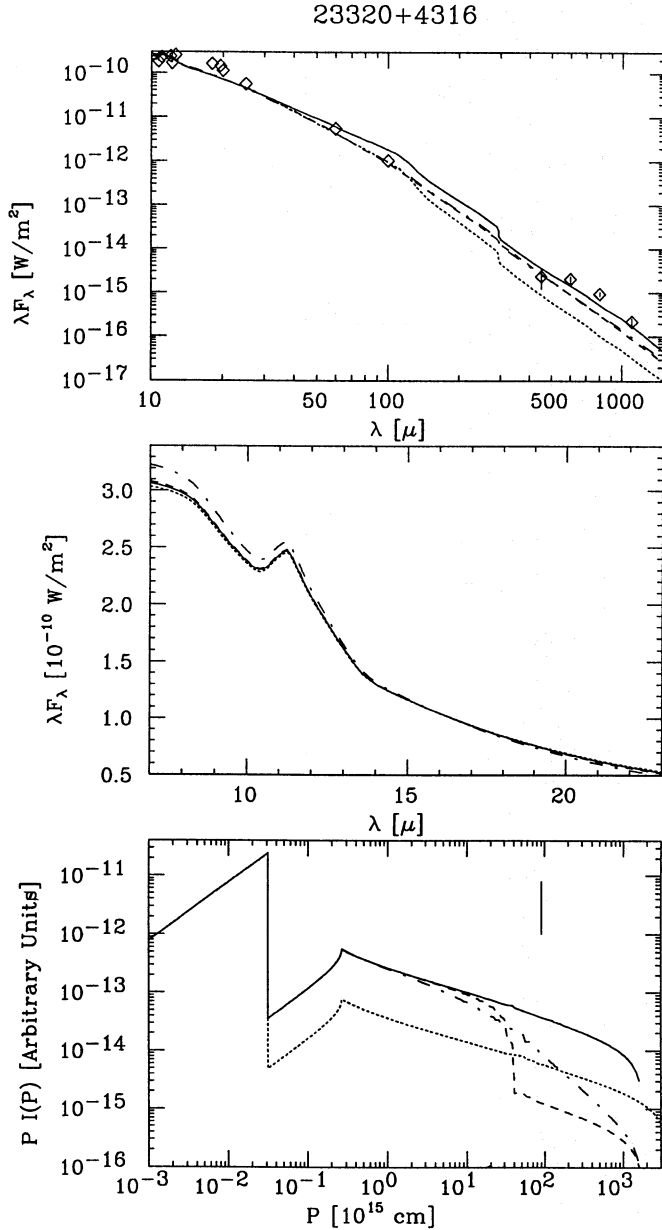
Fig. 26. The long-wavelength part of the SED (top panel), LRS spectrum (middle panel) and the brightness curve at 1 mm (bottom panel) for AFGL 3116. Along the x-axis of the brightness curve the impact parameter P is plotted ($P \approx 0.03$ corresponds to the stellar radius, $P \approx 0.25$ corresponds to the inner dust radius), along the y-axis P times the emerging intensity. The observed flux at earth is proportional to $\int_0^{p_{max}} I(P)P\,dP$. Indicated are the constant mass loss rate case (solid line), the thermal-pulse-type mass loss history (dashed line), the Bedijn-type mass loss history (dashed-dotted line) and a model with a steeper slope of the absorption coefficient (dotted line). In the SED the dashed and the dashed-dotted line are indistinguishable. The parameters are given in the text and are chosen to fit the IRAS 60 and 100 μm flux-densities. The LRS spectra have been normalised at 16 μm. The line in the bottom panel at $9\cdot 10^{16}$ cm represents the beam size of the JCMT telescope at 1 mm, at the assumed distance of AFGL 3116
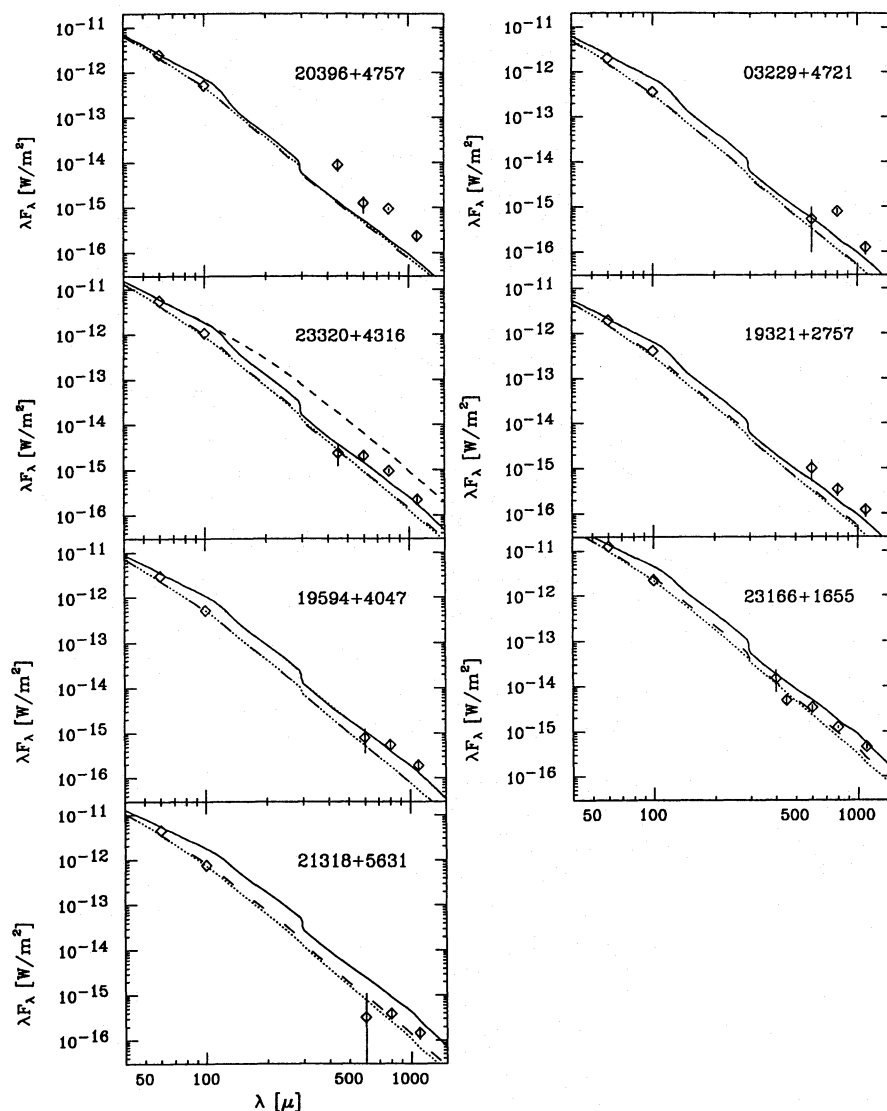
Fig. 27. The long-wavelength part of the SED for the stars where sub-mm data is available (1σ errors are indicated). The stars are plotted in order of increasing S_{25}/S_{12} ratio from left to right, and top to bottom. The solid line is the model with a constant mass loss rate. The dotted and the dashed line represent the models with a mass loss history related to thermal pulses and according to Bedijn (1987), respectively. These models are constructed to fit the IRAS 60 and 100 μm data. The break in the curves near 100 and 300 μm is due to beam effects. The short-dashed line in the panel for 23320+4316 represents the model with a constant mass loss rate without beam effects

For 17 stars in the sample, β ($Q_\lambda \sim \lambda^{-\beta}$ for $\lambda > 30\,\mu m$), f (for the Bedijn-type mass loss history) and Δt_1 (for the thermal-pulse-type mass loss history) are determined by fitting the IRAS 60 and 100 μm flux-densities. For $T_{\rm inn}$ the values in Table 2 are used. For some stars the present-day mass loss rate has been changed to give the same fit in the optical and NIR as for the constant mass loss rate case. The following range in values is found: $\beta = 1.2\text{-}1.9$, $f = 3\text{-}30$ and $\Delta t_1 = 340\text{-}2900$ yrs.

Changing f_1 to 20 or ∞ introduces a 20% change in Δt_1. Not surprisingly, the highest values for β and f and the lowest values for Δt_1 are found for the stars where the constant mass loss rate case predicts the highest 100 μm flux-density compared to the observations (cf. Fig. 25, middle and bottom panels).

The different models are illustrated in Fig. 26 for AFGL 3116, for which $\beta = 1.6$, $f = 11$ and $\Delta t_1 = 720$ yrs are derived. Since the absorption coefficient is changed only for $\lambda > 30\,\mu m$ there is no change in the LRS spectrum. With a higher value for β the fit at sub-mm wavelengths is noticeably worse than for the two mass loss history models (see the brightness curve in

the bottom panel of Fig. 26). This is found for all seven stars where sub-mm data is available to make the comparison.

The difference between the two mass loss histories is that the Bedijn-type history also changes the emission close to the star. This is demonstrated in the brightness curve and in the LRS spectrum where the Bedijn-type mass loss history gives the steepest slope. For AFGL 3116, with $f = 11$, this effect is not so large but for the most extreme carbon stars (with $f \gtrsim 20$) the Bedijn-type mass loss history predicts LRS spectra which are steeper than observed. Possibly this could be compensated for by changing $T_{\rm inn}$. Another effect of the Bedijn-type mass loss history is that the present-day mass loss rate is higher than that for the thermal-pulse-type mass loss history and the constant mass loss rate case. For AFGL 3116 this is only a 3% effect, for the most extreme carbon stars this amounts to 20%.

A combination of a steeper slope in the absorption coefficient and a mass loss history is also possible. For $\beta = 1.3$, which would fit the 60 and 100 μm data of all moderate infrared carbon stars, I find $f = 5$ and $\Delta t_1 = 1600$ yrs, for AFGL 3116. In

that case the Bedijn-type and the thermal-pulse-type mass loss history can fit the observations equally well.

The variation of β with C_{21} (cf. Fig. 25) could be interpreted, at first sight, as an increasing contribution of crystalline carbon (with $Q_\lambda \sim \lambda^{-2}$) relative to amorphous carbon (with $Q_\lambda \sim \lambda^{-1}$). Baron et al. (1987) find evidence that the proportion of crystalline to amorphous carbon *increases* with increasing temperature of the dust continuum, in agreement with the theoretical expectation (Gail & Sedlmayr 1984). This, then, would point to the mass loss history models rather than the steeper slope in the absorption coefficient as the correct model to explain the IRAS 60 and 100 μm flux-densities.

With both the Bedijn mass loss history and the mass loss history related to thermal pulses the observed IRAS 60 and 100 μm flux-densities can be fitted. The precise form of the mass loss rate history can not be derived from the present data, and may well be even different from the two mass loss rate histories considered here. The most powerful method to trace the density distribution of the dust, and thereby shed light on the possible mass loss history, is by mapping the circumstellar shell. This is illustrated in Fig. 26 for AFGL 3116 where the Bedijn-type mass loss history and the mass loss history related to thermal pulses predict the same sub-mm fluxes (top panel) but have different brightness curves (bottom panel). The optimum wavelengths for mapping the dust shell would be the far-infrared and the sub-mm and the required resolution would typically be <2″ (for a source at 0.7 kpc).

For all seven stars where sub-mm data is available the observations in the sub-mm wavelength range lie above the model predictions. This is illustrated in Fig. 27 where the long-wavelength part of the SED is plotted for the stars where sub-mm data is available. There are several possibilities to explain this discrepancy:

1. There is a contribution of CO line emission to the sub-mm fluxes. For IRC 10 216 this contribution at 1.3 mm has been estimated to be 40% (Walmsley et al. 1991). The deviations between the models and the observations are larger than a factor of 2 in the sub-mm range so this seems an unlikely explanation.
2. This is due to pulsational variability. This is unlikely, since the probability to observe seven stars above the mean flux level is only $(\frac{1}{2})^7 = 0.8\%$.
3. It may point to a detached shell, due to a phase of high mass loss in a distant past. Preliminary calculations show that this an unlikely explanation since any model that fitted the sub-mm fluxes predicted by far to much 60 and 100 μm flux. This is not surprising since the beam of the JCMT is small compared to the IRAS beam.
4. The sub-mm fluxes may sample a region where the circumstellar shell is slowed down by the interstellar medium, leading to a (relative) higher density and hence larger flux in the sub-mm range. This is unlikely for the same reason as (3). Mapping the outer parts of the circumstellar shell may provide information to which extent (3) and (4) contribute to the excess flux in the sub-mm region.
5. The excess in due to free-free emission. Since the beam of the JCMT is relatively small (corresponding to a radius of $1.4\ 10^{17}$ cm at 1 kpc or about 4500 stellar radii) compared to the extent of the circumstellar shell (about 50000 stellar radii), the excess is likely to originate in the inner parts of the circumstellar shell. Previously, free-free emission has been proposed to (partly) account for the flux beyond 3.3mm in IRC 10 216 (Griffin 1990). To investigate if, and to which extent, free-free emission is indeed responsible for the sub-mm excess would require sub-mm data with a better S/N than the present data, observations in the cm region and theoretical modelling.

References

Alknis A., 1980, Investigations of the sun and red stars 11, 5

Baron Y., de Muizon M., Papoular R., Pégourié B., 1987, A&A 186, 271

Baud B., Habing H.J., 1983, A&A 127, 73

Bedijn P.J., 1987, A&A 186, 136

Bergeat J., Sibille F., Lunel M., Jefevre J., 1976, A&A 52, 227

Blanco A., Fonti S., Rizzo F., 1991, Infrared Physics 31, 167

Borghesi A., Bussoletti E., Colangeli L., De Blasi C., 1985, A&A 153, 1

Cardelli J.A., Clayton G.C., Mathis J.S., 1989, ApJ 345, 245

Chan S.J., Kwok S., 1990, A&A 237, 354

Cohen M., Kuhi L.V., 1977, PASP 89, 829

Cohen M., Walker R.G., Witteborn F.C., 1992, AJ 104, 2030

Dyck H.M., Lockwood G.W., Capps R.W., 1974, ApJ 189, 89

Egan M.P., Leung C.M., 1991, ApJ 383, 314

Epchtein N., et al., 1987, A&AS 71, 39

Epchtein N., Le Bertre T., Lépine J.R.D., 1990, A&A 227, 82

Fleischer A.J., Gauger A., Sedlmayr E., 1992, A&A 266, 321

Forrest W.J., Houck J.R., McCarthy J.F., 1981, ApJ 248, 195

Fouqué P., Le Bertre T., Epchtein N., Guglielmo F., Kerschbaum F., 1992, A&AS 93, 151

Frogel J.A., Cohen J.G., Persson S.E., Elias J.H., 1981, in: Physical Processes in Red Giants Stars, eds. I. Iben, A. Renzini, Reidel, Dordrecht, p. 159

Gail H.-P., Sedlmayer E., 1984, A&A 132, 163

Goebel J.H., Moseley S.H., 1985, ApJ 290, L35

Grasdalen G.L., Gehrz R.D., Hackwell J.A., Castelaz M., Gullixson C., 1983, ApJS 53, 413

Griffin I.P., 1990, MNRAS 247, 591

Griffin I.P., 1993, MNRAS 260, 831

Groenewegen M.A.T., 1993, Chapter 5, Ph.D. thesis, University of Amsterdam

Groenewegen M.A.T., de Jong T., 1991, ESO Messenger 66, 40

Groenewegen M.A.T., de Jong T., 1993, A&AS 101, 267

Groenewegen M.A.T., de Jong T., 1994, A&A 281, 115

Groenewegen M.A.T., de Jong T., Baas F., 1993, A&AS 101, 513

Groenewegen M.A.T., de Jong T., Geballe T.R., 1994, A&A, in press
Groenewegen M.A.T., de Jong T., van der Bliek N.S., Slijkhuis S., Willems F.J., 1992, A&A 253, 150 (paper I)
Guglielmo F., et al., 1993, A&AS 99, 31
Joint IRAS Science Working Group, 1986, IRAS catalogs and atlases, Low Resolution Spectrograph (LRS), A&AS 65, 607
Joint IRAS Science Working Group, 1986, IRAS catalogs and atlases, Point Source Catalog (PSC), US Government Printing Office, Washington
Joint IRAS Science Working Group, 1986, IRAS catalogs and atlases, Explanatory Supplement, US Government Printing Office, Washington
Jones T.J., et al., 1990, ApJS 74, 785
Jura M., 1986, ApJ 303, 327
Justtanont K., Tielens, A.G.G.M., 1992, ApJ 389, 400
Kholopov P.N., et al., 1985, General Catalog of Variable Stars (GCVS), Nauka, Moscow
Le Bertre T., 1987, A&A 176, 107
Le Bertre T., 1988, A&A 203, 85
Le Bertre T., 1992, A&AS 94, 377
Lebofsky M.J., Rieke G.H., 1977, AJ 82, 646
Lockwood G.W., 1974, ApJ 192, 113
Lopez B., Perrier C., Mékarnia D., Lefèvre J, Gay J., 1993, A&A 270, 462
Loup C., Forveille T., Omont A., Paul J.F., 1993, A&AS 99, 231
Low F.J., Kurtz R.F., Vrba F.J., Rieke G.H., 1976, ApJ 206, L153
Martin P.G., Rogers C., 1987, ApJ 322, 374
Meadows P.J., Good A.R., Wolstencroft R.D., 1987, MNRAS 225, 43P
Mitchell R.M., Robinson G., 1980, MNRAS 190, 669
Neckel Th., Klare G., 1980, A&AS 42, 251
Noguchi K., et al., 1981, PASJ 33, 373
Onaka T., de Jong T., Willems F.J., 1989, A&A 218, 169
Orofino V., Colangeli L., Bussoletti E., Blanco A., Fonti S., 1990, A&A 231, 105
Papoular R., 1988, A&A 204, 138
Parenago P.P., 1940, Astron. Zh. 17, 3
Pégourié B., 1988, A&A 194, 335
Ridgway S.T., Keady J.J., 1988, ApJ 326, 843
Rouleau F., Martin P.G., 1991, ApJ 377, 526
Rowan-Robinson M., Harris S., 1983a, MNRAS 202, 767
Rowan-Robinson M., Harris S., 1983b, MNRAS 202, 797
Rowan-Robinson M., Lock T.D., Walker D.W., Harris S., 1986, MNRAS 222, 273
Sahai R., Wootten A., Clegg R.E.S., 1984, ApJ 284, 144
Schutte W.A., Tielens A.G.G.M., 1989, ApJ 343, 369
Sopka R.J., et al., 1985, ApJ 294, 242
Tielens A.G.G.M., 1990, in: From miras to planetary nebulae, eds. M.O. Mennessier, A. Omont, Editions Frontieres, Gif-sur-Yvette, p. 186
van der Bliek N.S., 1988, M.Sc. thesis, University of Amsterdam
van der Veen W.E.C.J., 1989, A&A 210, 127
Walmsley C.M., et al., 1991, A&A 248, 555
Willems F.J., de Jong T., 1988, A&A 196, 173
Zijlstra A.A., Loup C., Waters L.B.F.M., de Jong T., 1992, A&A 265, L5

underestimated by Walmsley et al. (1991) and is more like 55%. In addition they show that line emission contributes $\gtrsim 65\%$ to the broadband flux in the 345 GHz window in CW Leo.

It appears that molecular line emission is in fact an important contributor to the observed submm broadband fluxes.

Note added in proof: In a recent preprint, Groesbeck, Phillips and Blake (Caltech submillimeter observatory preprint; submitted to ApJS) argue that the contribution of molecular line emission to the total submm flux in the 230 GHz passband was